communications
earth & environment

ARTICLE

https://doi.org/10.1038/s43247-021-00203-w OPEN

Dominant role of vertical air flows in the unprecedented warming on the Antarctic Peninsula in February 2020

Min Xu[1], Lejiang Yu[2], Kaixin Liang[1], Timo Vihma[3], Deniz Bozkurt[4], Xiaoming Hu[1] & Qinghua Yang[1✉]

Near-surface air temperature at the Argentinian research base Esperanza on the northern tip of the Antarctic Peninsula reached 18.3 °C on 6 February 2020, which is the highest temperature ever recorded on the entire Antarctic continent. Here we use weather observations since 1973 together with the ERA5 reanalysis to investigate the circulation that shaped the 2020 event, and its context over the past decades. We find that, during the 2020 event, a high-pressure ridge over the 40°-100°W sector and a blocking high on the Drake Passage led to an anticyclonic circulation that brought warm and moist air from the Pacific Ocean to the Antarctic Peninsula. Vertical air flows in a foehn warming event dominated by sensible heat and radiation made the largest contribution to the abrupt warming. A further analysis with 196 extreme warm events in austral summer between 1973 and 2020 suggests that the mechanisms behind the 2020 event form one of the two most common clusters of the events, exhibiting that most of the extreme warm events at Esperanza station are linked to air masses originating over the Pacific Ocean.

---

[1] School of Atmospheric Sciences, Sun Yat-sen University, and Southern Marine Science and Engineering Guangdong Laboratory (Zhuhai), Zhuhai, China. [2] MNR Key Laboratory for Polar Science, Polar Research Institute of China, Shanghai, China. [3] Finnish Meteorological Institute, Helsinki, Finland. [4] Department of Meteorology, University of Valparaíso, Valparaíso, and Center for Climate and Resilience Research (CR)2, Santiago, Chile. ✉email: yangqh25@mail.sysu.edu.cn

The Antarctic Peninsula (AP) is the northernmost tip of Antarctica and has the mildest climate within the continent. Observations have shown remarkable temperature changes in the AP, with a significant warming trend in near-surface air temperature between 1950s and 2000[1,2] and cooling since then[3,4]. The AP temperature changes impact the ecosystems, the mass balance of the ice shelves and upstream glaciers[5–8], hence, also the global sea level[9].

The AP cordillera acts as an orographic obstacle to the westerly winds, leading to two different climatic zones: a relatively mild and humid marine climate on the west coast and a cooler continental climate on the east coast[10,11]. There are different factors in warm events over the two sides of the AP. The warming on the northwest side has been linked to strengthened northerly flow due to the increasing South Atlantic pressure and the deepening Amundsen Sea low[12,13], which are largely caused by a Rossby wave train associated with tropical Pacific sea surface temperature anomalies[14]. On the northeast side, strong circumpolar westerlies resulted from the positive Southern Annular Mode facilitate the occurrence of dry and warm descending winds (i.e., Foehn), which have an important influence on the warming[15–21].

The Argentine Esperanza Base (63.4°S, 57°W) meteorological station is located on the northeastern tip of the AP, at an elevation of 24 m asl. The station is on the eastern shore of Hope Bay. Stretching along the opposite side of the bay is Ami Boué Peak of about 1100 m high, southwest to the station. The near-surface air temperature variations of Esperanza station have been investigated over the last decade. Stastna et al.[22] and Turner et al.[13] reported a summer temperature trend of 0.4 °C per decade during 1952–2003 and about 0.29 °C per decade for 1945–2018 respectively. Mulvaney et al.[23] documented a warming trend for the period from 1958 to 2008 that would equate to about 3.5 °C per century. In addition to the long-term warming trends, the station has experienced episodic extreme warm events. For instance, an extreme temperature of 17.5 °C was recorded on 24 March 2015[24]. It was due to a foehn event triggered by an atmospheric river[25].

Recently, on 6 February 2020, the 2 m temperature at Esperanza station increased up to 18.3 °C. It is the highest temperature ever recorded on the entire Antarctic continent. Concurrently, the 2019/2020 summer resulted in record-breaking surface melt in the Larsen C Ice Shelf[26], and air temperatures over some parts of the AP (i.e., northern George VI Ice Shelf) were continuously ≥0 °C for anomalously long time periods, particularly in early February 2020[27]. Although Bozkurt et al.[25] mentioned the contribution of heat advection to the warming in March 2015, little attention has been paid to the thermodynamic mechanism of warm extremes. In this study, we examine how the horizontal heat advection, vertical motion, and diabatic heating collectively shaped the record-high temperature in 2020.

Results

The extreme warm event and associated atmospheric circulation. Figure 1 shows the variations of 2 m temperature, wind speed, wind direction and relative humidity at Esperanza station from 1 to 9 February 2020. The time series highlight the extreme temperature on 6 February. At 15 UTC on 6 February, the 2 m temperature increased up to 18.3 °C. Between 6 and 15 UTC on 6 February, the temperature rose dramatically from −0.7 to 18.3 °C in 9 h, with an extreme warming rate of 4 °C h^{-1} at the end of the period. A secondary peak of 17.3 °C was observed at 21 UTC on 6 February. High temperatures on 6 and 7 February were accompanied by a rapidly increased wind speed (from 1.5 to 19 m s^{-1}) with a southwesterly direction as well as the simultaneously decreased relative humidity (from 90.5 to 22.6%). Considering the station is located at the lee side of a mountain barrier, it is reasonable to infer that a warm and dry downslope wind (foehn) contributed to the warming. By 8 February, the temperature returned to levels similar to those before the event. The spatial distribution of 2 m temperature anomalies with a reference to the daily climatology of 1979–2020 (Fig. 2) shows positive anomalies

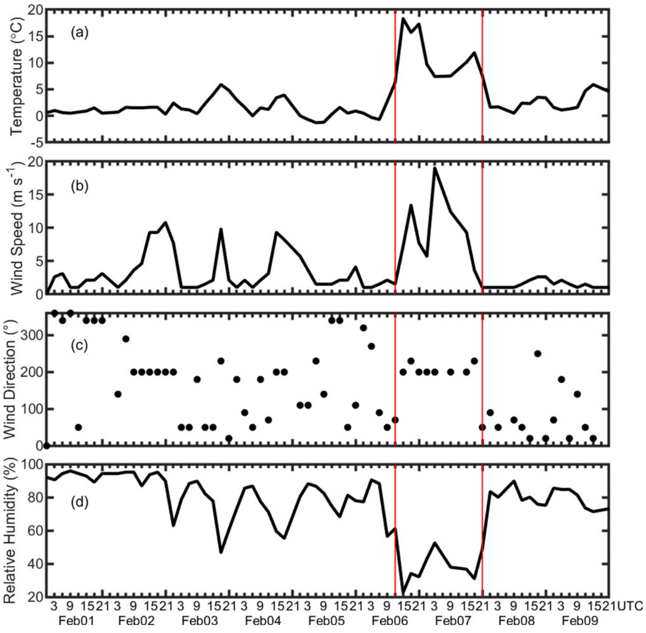

Fig. 1 Time series of three-hourly surface observations at Esperanza station. a 2 m air temperature, **b** wind speed, **c** wind direction and **d** relative humidity from 1 to 9 February, 2020. The period of the early February warming is indicated by the red lines.

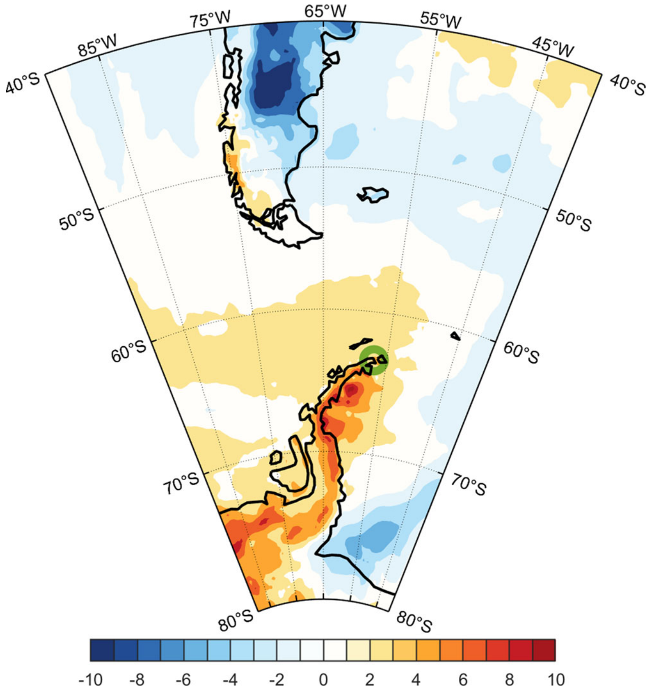

Fig. 2 Spatial distribution of 2 m temperature anomaly. ERA5 temperature anomalies (°C) at 15 UTC on 6 February 2020 are calculated with respect to the long-term daily 2 m temperature climatological mean (6 February, 15 UTC) during 1979–2020. Esperanza station is marked with a green circle.

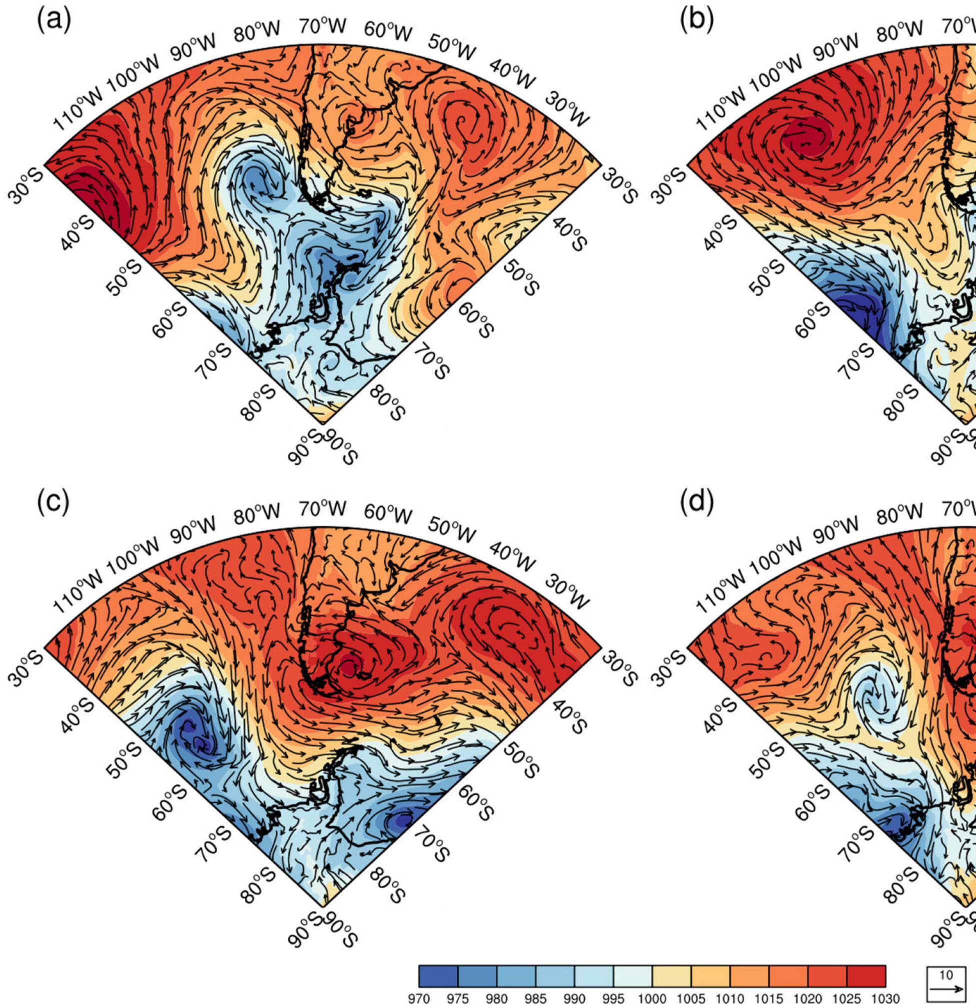

Fig. 3 Atmospheric circulation evolution in near-surface layers. ERA5 mean sea level pressure (hPa, shaded) and 10 m wind (m s^{-1}, arrows) at 15 UTC on 2 (**a**), 4 (**b**), 6 (**c**) and 8 (**d**) February, 2020.

over the entire AP, with large anomalies covering more area on the eastern side.

To illustrate the synoptic-scale circulation in near-surface layer and mid-troposphere during this extreme high temperature event, Figs. 3 and 4 display the mean sea level pressure and 10 m wind fields as well as 500 hPa geopotential height and wind fields every other day from 2 to 8 February 2020. Similar patterns are seen in both figures. Before the rise of 2 m air temperature, synoptic-scale cyclones appeared near the southwestern coast of South America on 2 February, and they moved over the Weddell Sea after 4 February. Meanwhile, a high-pressure ridge moved eastward from the southeastern Pacific Ocean to the Bellingshausen Sea, along with a cold trough of low pressure over southern South America on 4 February. At the time of the warming on 6 February, the mean sea level pressure and 10 m wind field comprised high pressure centered over the southeast to South America and low pressure over the southeastern Pacific Ocean leading to the southwesterly flow to the station. As to the 500 hPa pattern, there was a blocking high over the Drake Passage on 6 February, disrupting the prevailing westerly circumpolar flow, and resulting in deepening and northward expansion of Amundsen Sea low. This synoptic configuration was instrumental to the transport of warm air masses along the southern periphery of the anticyclone from the Pacific Ocean to the Bellingshausen Sea and the AP. By 8 February, a weak cyclone appeared again over the ocean to the southwest of South America, and the blocking was deformed to a high-pressure ridge, which shifted eastward. The 500 hPa circulation pattern consisted of the north-south oriented ridge flanked by two low-pressure systems on either side.

As seen in Figs. 3 and 4, the maximum intensity of the ridge affecting the air temperature occurred from 6 to 8 February. Anomalies of the 500 hPa geopotential height and wind fields averaged over these 3 consecutive days are shown in Fig. 5. The anomalies were calculated with respect to the mean values of the same 3 days over the 1979–2020 period. The circulation was characterized by a tropospheric anticyclonic flow anomaly over the Drake Passage, which was coupled with subsiding air masses. The positive geopotential height anomaly over the AP indicates a wide high-pressure system there, as the blocking high prevailed. Around Esperanza station, the 500 hPa geopotential height anomaly was about 300 gpm, about 2.5 times the standard deviation of climatological value.

Contributions of thermodynamic processes to the temperature variation. To quantify the contributions of horizontal advection, vertical motion, and diabatic heating to the local temperature change, the thermodynamic equation[28] was applied to calculate the three terms. (Eq. 1) Their variations at 975 hPa near the station (the nearest grid point at 63.5°S, 57°W) from 1 to 9 February are shown in Fig. 6. On 6 February, the warming was dominated by the vertical motion term, including the effects of

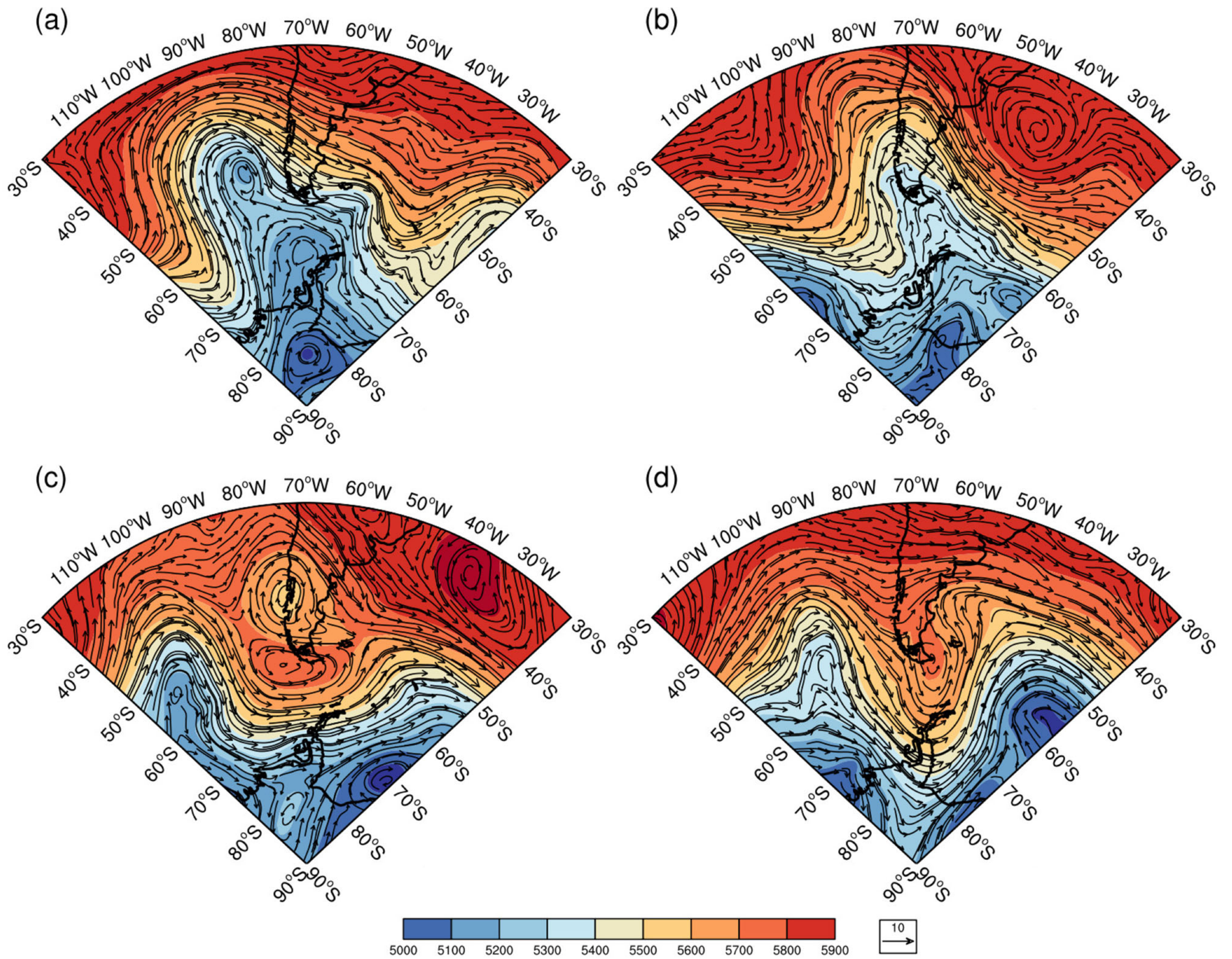

Fig. 4 Atmospheric circulation evolution in mid-troposphere. ERA5 500 hPa geopotential height (gpm, shaded) and wind (m s^{-1}, arrows) at 15 UTC on 2 (**a**), 4 (**b**), 6 (**c**) and 8 (**d**) February, 2020.

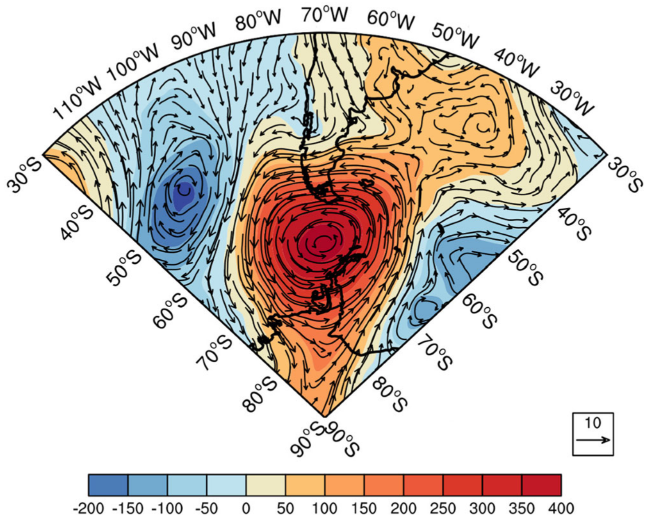

Fig. 5 Anomalous 500 hPa geopotential height and wind. ERA5 geopotential height (gpm, shaded) and wind (m s^{-1}, arrows) anomalies are averaged during 6–8 February in 2020 with respect to the mean values of the 3 consecutive days over the 1979–2020 period.

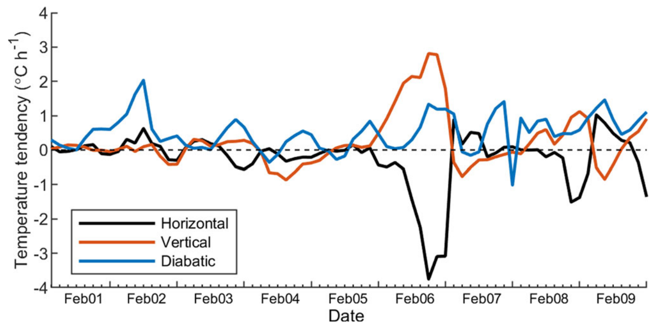

Fig. 6 Time series of temperature changes from three terms. The contributions of horizontal advection (black line), vertical motion (red line) and diabatic heating (blue line) to temperature variations at 975 hPa obtained from ERA5 for a grid point near the station from 1 to 9 February, 2020.

adiabatic heating ($\omega \frac{RT}{c_p p}$) and vertical advection ($-\omega \frac{\partial T}{\partial p}$). At the same time, the diabatic heating also contributed to the temperature increase, but was balanced by the horizontal cold-air advection. The negative influence of horizontal advection indicates that the southwest winds advected cold-air masses to the station while the warm air masses along the ridge mainly affected

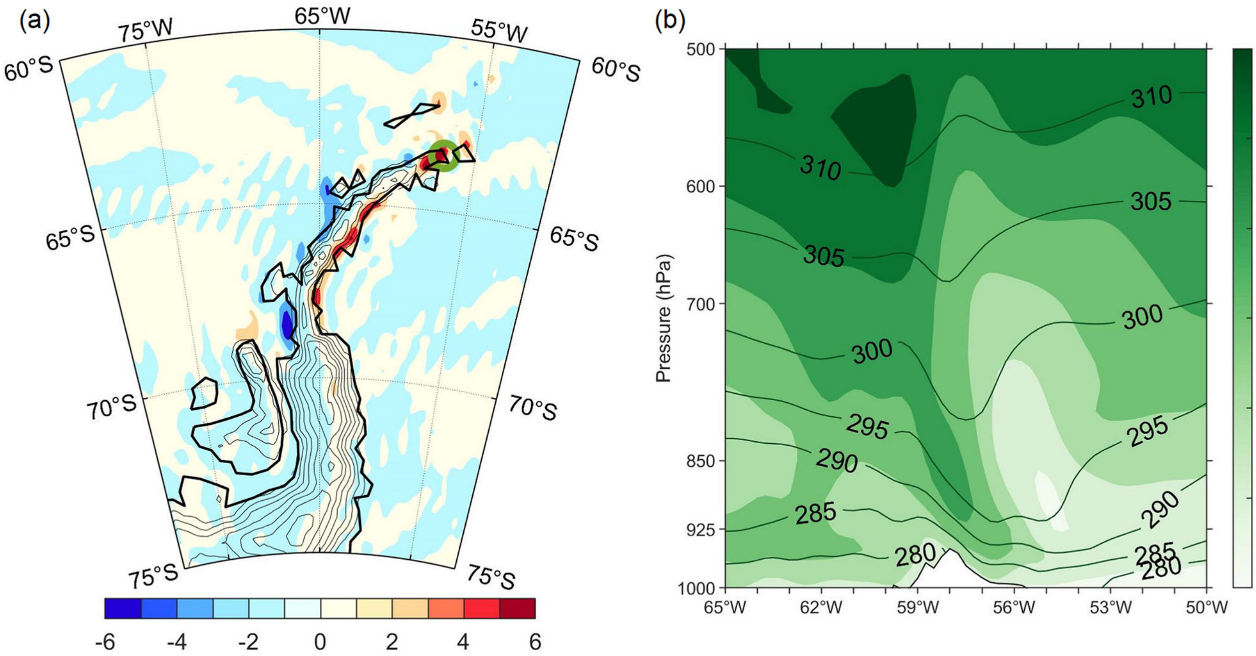

Fig. 7 Spatial distribution of vertical terms and vertical cross section of the wind speed and potential temperature at 63.5°S. a ERA5 temperature change (°C h^{-1}, shaded) from the vertical term over the AP at 925 hPa at 15 UTC on 6 February, 2020. Surface geopotential heights are drawn by contour lines with 200 m intervals. Esperanza station is marked with a green circle. **b** ERA5 vertical cross section of wind speed (m s^{-1}, shaded) and potential temperature (K, contour lines) between 50°W and 65°W around the station at 15 UTC on 6 February, 2020. The white area marks the mountain according to the surface geopotential height from ERA5.

the Bellingshausen Sea. The variation in the diabatic term was relatively small. In brief, vertical motion was the primary factor of the temperature increase. The descending air masses provided a favorable condition for the adiabatic warming.

The spatial distribution of temperature changes due to vertical motion and the cross section of the wind speed and potential temperature around Esperanza station (around 63.5°S) were further examined (Fig. 7). Considering the near-surface pressure in the vicinity of the station, we chose a slightly higher level of 925 hPa. The vertical temperature gradient was calculated from the difference between temperatures at the 850 and 975 hPa levels. Compared with other days during 1–9 February 2020, on 6 February, when the vertical motion term was strongest, there were obvious differences between the east and west side of the AP. On the northeastern side, the vertical term had intense warming rates around the station, faster than values in most other areas. In contrast with the west side, vertical motion played an important role in the warming of the east side confined to the shores. At the same time O'Higgins station almost at the same latitude as Esperanza station on the west side recorded a temperature of 1.7 °C, indicating no occurrence of extreme temperatures. These observed temperature differences between the east and west side of the northern tip of the AP match the pattern in Fig. 7a and indicate the role of local orography and foehn effect. Comparing the vertical dynamical and thermodynamic structure of the two sides at 15 UTC on 6 February in Fig. 7b, the wind speed on the leeward slope was larger than that on the windward side, as the upslope wind moved slowly and sped up in downslope motion at about 925 hPa. Accompanied by the winds advecting the upper air downward, the relatively dense contours of potential temperature above the lee slope descend along the mountain barrier, indicating an isentropic drawdown on the lee side of the AP.

We then quantified the heat budget to find out what caused the foehn warming at the station. The foehn mechanisms include (a) isentropic drawdown, when warm and dry air is advected isentropically down the lee slopes, (b) thermodynamic mechanism that latent heating and precipitation during air ascending on the windward slopes, and (c) sensible heat flux and radiative heating along the lee side. The foehn warming is the temperature change induced by these mechanisms and the cross-mountain pressure gradient. As a lee side low pressure anomaly is generated during a foehn event, leading to a minor lee side cooling[29]. Our calculations were based on output of the Lagrangian trajectory model. Figure 8 shows the 24 h backward trajectory and the air temperature change along the path. The foehn warming is 4 K. Contributions from each mechanism comprise isentropic drawdown of 0.6 K, thermodynamic mechanism of −0.6 K, sensible heat and radiation of 5.7 K, and pressure gradient of −1.7 K. In this event, the contribution of isentropic drawdown to the warming was small, indicating that the approaching winds were strong enough to propel the low-level air up and over the mountain barrier. The height of point B was about 120 m, confirming that the source of air was at the low-level. The dominant contribution was found to be sensible and radiative heating. Mechanical mixing was amplified when wind sped up, leading to a convergence of the sensible heat flux. The contributions of latent heating and pressure gradient were negative during the event.

We further analyzed the integrated water vapour transport. Consequently, there was an atmospheric river toward the AP on 6 February (Supplementary Fig. 1) but it was not strong enough to trigger foehn warming by latent heating, consistent with the result of heat budget analysis. A much stronger atmospheric river with a large water vapour transport occurred in March 2015 (Supplementary Fig. 2) when the high temperature was observed.

Climatological analyses of extreme warm events. We examined a collection of 196 extreme warm events in summer (December to

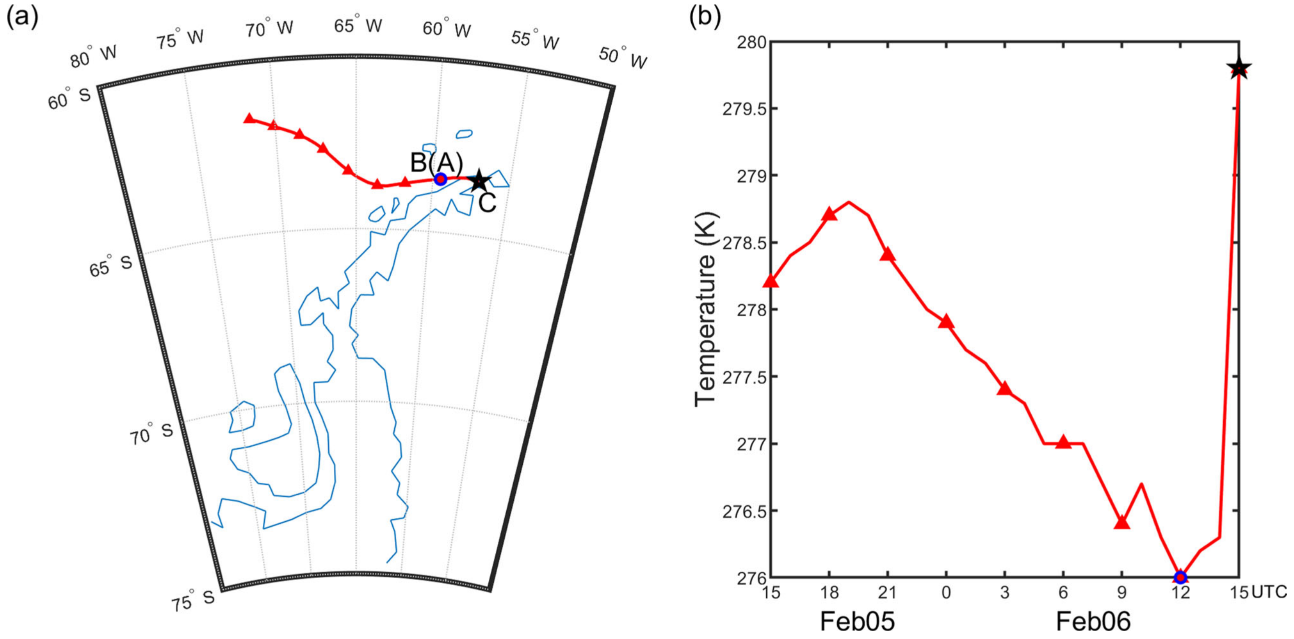

Fig. 8 The 24 h backward trajectory and the air temperature change along the path. **a** The 24 h backward trajectory of air mass involved in the 2020 event. The star marker (Point C) is the station. The blue circle (Point B/A) is air mass at 12 UTC with a distance of the Rossby radius of deformation to the mountain. **b** The air temperature (K) along the path. The star marker and blue circle indicate the same points as those in (**a**).

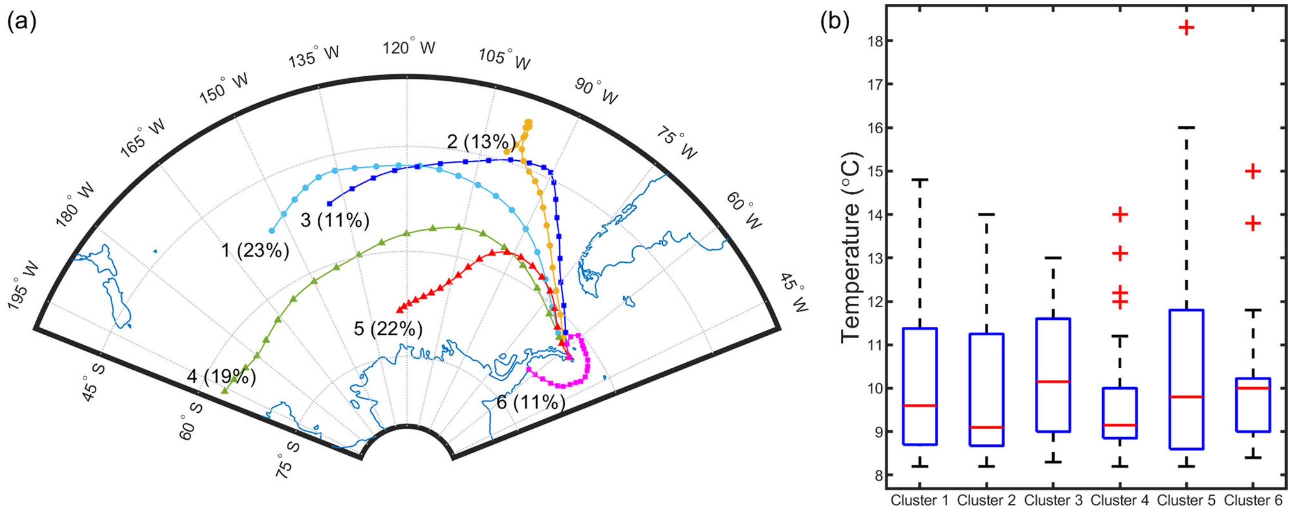

Fig. 9 Average 10-day backward trajectories and boxplot of the extreme temperatures for six clusters. **a** The air mass trajectories of extreme warm events in summer during 1973–2020 are classified into six types with respective proportions in brackets. **b** Boxplot of extreme summer temperatures for six clusters. The red center lines are the medians. The vertical dashed lines (whiskers) indicate the variability outside the lower and upper quartiles. The red crosses represent outliers.

February, see the Methods) to provide some climatological context and the characteristics of such events for this region. To ascertain the different sources of the air masses during these events since 1973 and compare them with the event of February 2020, a cluster analysis was used to classify the 10-day backward trajectories of the air masses. The mean trajectories and boxplot of extreme temperatures for six clusters are shown in Fig. 9. The six trajectories reveal that most air masses (89%) involved in the extreme events at Esperanza station originated from about 500 to 1500 m above the Pacific Ocean, crossing the Drake Passage. The westernmost air masses of more than 135° longitude (~6710 km) away from the station were Cluster 4 with the lowest 75th percentile temperature, and the northernmost air masses originated from near 45 °S (~2050 km) were Cluster 2 with the lowest median of temperature in relation to the medians of the other five clusters. The most recurved trajectory from the Pacific sector was Cluster 5 with a proportion of about 22%. This cluster includes the event of February 2020. Its origin was closest to the station among the trajectories from the west. Cluster 5 had the highest 75th percentile temperature and maximum value with the outlier of 18.3 °C. Cluster 6 (11% of cases) was an entirely different type of trajectories, associated with an anticyclonic circulation over the northwestern Weddell Sea. In brief, air parcels moving from the west on a relatively short route can be more favorable for high summer temperatures.

In light of the above, we infer that common characteristic can be found in the circulation of the extreme events. The anomaly field of the 500 hPa geopotential height for the extreme warm

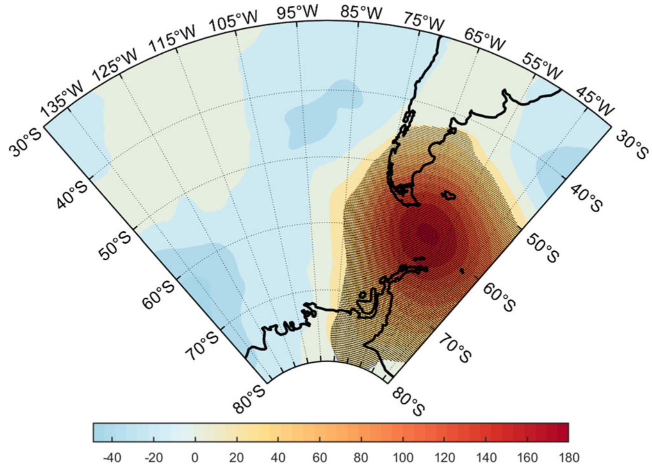

Fig. 10 Composite of 500 hPa geopotential height anomaly. ERA5 anomalies (gpm) for the extreme warm events in Cluster 5 are calculated with respect to the 1979–2020 period. The shaded area indicates regions where the anomalies are statistically significant at 95% confidence level.

events in Cluster 5 (Fig. 10) reflects the importance of the positive pressure anomaly over the Drake Passage. The positive departures from the mean climatological 500 hPa height resemble the anomaly field of the February 2020 event in Fig. 5. In the other clusters of warm events, the 500 hPa height patterns also had similar magnitude of positive anomaly with slightly different locations in different clusters. The trajectories and composite analyses imply that to a large extent, the extreme warm events in summer can be related to an inflow of marine air and the development of a tropospheric ridge.

Conclusions

A record-warm event occurred on the northeastern tip of the AP, where a 2 m air temperature of 18.3 °C was observed at Esperanza station on 6 February 2020. The evolution of the circulation responsible for the exceptional temperature rise was investigated using ERA5 reanalysis data. In terms of the variations of the sea level pressure, 500 hPa geopotential height and wind patterns, the high-pressure ridge and the blocking high over the Drake Passage led to a circulation that advected warm air masses to the northern AP. The atmospheric circulation during previous extreme warm events has been analyzed in several studies. The warm event in December 1997 occurred when a passing mid-tropospheric ridge reached the interior of West Antarctica, and the related anticyclonic circulation advected warm air to the Patriot Hills area[30]. As to the warm event at Esperanza station in late March 2015, a deep low-pressure center over the Amundsen–Bellingshausen Sea and a blocking ridge over the southeast Pacific directed warm, moist air to the AP[25].

To explain the driver of the record-warm event, the thermodynamic equation was applied to quantitatively calculate the contributions of horizontal advection, vertical motion and diabatic term to the temperature variation. The results demonstrate that the vertical motion was the main contributor to the temperature increase, while the effect of horizontal advection on the temperature was negative, indicating the horizontal advection of cold-air masses from the southwest. Although a ridge to the Bellingshausen Sea on 6 February increased the chance of large-scale warm air advection toward the AP, the local-scale forcing was found to be more pronounced during the event because the warm air encountered the AP barrier, and acted on the station as vertical flows (foehn). In the heat budget analysis, sensible heat and radiation were the dominant mechanisms for foehn warming on 6 February. The foehn conditions tend to be associated with well-developed low-pressure systems in the Amundsen–Bellingshausen Seas[18]. In this respect, there was also a deepening Amundsen Sea low in this event shown in the evolution of circulation.

In view of all the extreme summer high temperatures at the station, the 10-day backward trajectories calculated by the HYSPLIT model allow the identification of the air mass origins and pathways. The cluster analysis of the trajectories reveals that the air masses toward Esperanza station during extreme warm summer events in 1973–2020 mostly originated over the Pacific Ocean. As to the 500 hPa geopotential height anomaly fields of these extreme warm events, high pressure is the typical large-scale circulation characteristic similar to that depicted in the February 2020 event. The positive anomaly is coincident with the previous research that positive temperature anomalies on the northeast peninsula in summer are associated with positive pressure anomalies north of the AP[17].

The warming trend in the AP weakened during the last 20 years, nonetheless, Esperanza station has still experienced extreme warm events given its special geographical location as the northernmost station of the Antarctic continent. Baroclinic midlatitude systems and westerlies can favor the moisture transport and warm air advection from the lower latitudes toward the northeast Peninsula. In addition, Esperanza station is located on the leeward side of a mountain, providing favorable conditions for the occurrence of foehn winds. It is expected that similar high temperatures may be recorded in the future.

Due to the limited spatial resolution of ERA5, our study of foehn may be inadequate in detail but, in the case of the February 2020 event, the air mass transport to Esperanza station and the temperature change along the trajectory seem to be reasonably well captured to explain the key mechanisms responsible for the record-warm event. Higher-resolution numerical simulations are needed to better resolve all mechanisms affecting meteorological variables and their interaction with the ocean and cryosphere in the complex AP environment.

Methods

Data. The surface observations of air temperature, wind speed, wind direction, and relative humidity (calculated on the basis of temperature and dew point temperature) at Esperanza station were taken from the Integrated Surface Database accessed from the NOAA's National Climatic Data Center. It consists of global hourly surface weather observations from numerous sources[31]. The data have undergone an automated and comprehensive quality control[32] and have been employed widely for climate analysis[33–35]. The available observations recorded at Esperanza station are 3-hourly since 1973.

The atmospheric circulation affecting the AP was analyzed based on the ERA5 reanalysis, which is the most recent reanalysis product of the European Center for Medium-Range Weather Forecasts that combines large amounts of historical observations into global estimates using advanced modeling systems and data assimilation[36,37]. ERA5 is highly accurate, representing the magnitude and variability of near-surface air temperature and wind regimes over the Antarctic continent[11,38–40]. ERA5 provides hourly data with a spatial resolution of 0.25° × 0.25° and a vertical resolution of 37 pressure levels (1000 hPa to 1 hPa, surface to about 50 km in the area of Esperanza) from 1979 to present. Variables we used from ERA5 are the 2 m temperature, 10 m wind components, mean sea level pressure, 500 hPa geopotential height and wind components, 850 hPa temperature and geopotential height, temperature, wind and vertical velocity at 925 hPa and 975 hPa, as well as surface pressure and geopotential. As no remarkable changes of circulation patterns occurred on time scales shorter than a day, we employed the large-scale circulation fields at 15 UTC (the time when the peak temperature occurred on 6 February) for each day to represent the synoptic patterns.

Meteorological analyses. The temperature tendency is described by the thermodynamic equation[28]:

$$\frac{\partial T}{\partial t} = -V\cdot\nabla T + \left(\frac{RT}{c_p p} - \frac{\partial T}{\partial p}\right)\omega + \frac{J}{C_p} \tag{1}$$

On the right-hand side of Eq. (1), the first term is the horizontal advection $-V\cdot\nabla T = -[\mathrm{u}(\partial T/\partial x) + \mathrm{v}(\partial T/\partial y)]$, which represents the intensity of the horizontal heat transport depending on the wind speed and the temperature gradient. It was calculated using the wind and air temperature in ERA5. The second term indicates the temperature change due to vertical motion. R is the gas constant. c_p is the specific heat at constant pressure. $\partial T/\partial p$ at the 975 hPa level was calculated from the difference of temperature between the 850 hPa level and 2 m above ground level. ω is the vertical velocity (Pa s^{-1}). The third term is diabatic heating including shortwave and longwave radiation as well as latent and sensible heat. The temperature tendency due to shortwave and longwave radiation used here was taken from the deterministic forecast of the atmosphere model at the lowest level (137) of ERA5. The latent heating was estimated from the ERA5 precipitation assuming that 1 mm h^{-1} yields ~1.5 K of heating[41]. As to the surface sensible heat, assuming that the sensible heat flux (F_H) decreases linearly from its surface value to zero by the top of the atmospheric boundary layer[42], the contribution is $-\frac{1}{\rho c_p}\frac{\partial F_H}{\partial z}$, where ρ is the air density[43]. The sensible heat flux and the boundary layer height are available in ERA5.

To identify all the extreme warm events, we extracted daily maximum temperature in the austral summer (December to February) from December 1973 to February 2020. Data in 1979, 2004, and 2005 were missing. The 95 Percentile of the distribution was used as a threshold for extreme warm events. The Hybrid Single-Particle Lagrangian Integrated Trajectory (HYSPLIT) model[44] from the Air Resources Laboratory was used to calculate the air mass backward trajectories of the events. HYSPLIT is one of the most widely used atmospheric transport and dispersion models for trajectory calculations to determine the air mass origins and pathways. The HYSPLIT model was further employed for the heat budget analysis and cluster analysis of the trajectories. To simplify the analyses, multiple trajectories that share some commonalities in space were aggregated into groups, called clusters, and represented by their mean trajectory. Doing so, the differences between trajectories within a cluster were minimized while differences between clusters were maximized. Computationally, trajectories were combined until the total variance of the individual trajectories about their cluster-mean started to increase substantially[45].

We analyzed the heat budget using the Lagrangian trajectory model output to quantify the causes of foehn warming. The calculation is based on temperature T, potential temperature θ, and calculated equivalent potential temperature θe at three points[29]. Point C is at the station (Fig. 8, star marker). Following the flow backward, point B (Fig. 8, blue circle) is in the undisturbed flow at a distance farther than the Rossby radius of deformation (at the AP of about 150 km) from the mountain[29]. It is at 12 UTC with a height of 124 m. Point A is below point B, 2 m above the ground level as point C. The temperature at point A is the 2 m temperature from ERA5. The contributions include (i) Isentropic drawdown $\Delta^{ID}T = \theta_B - \theta_A$; (ii) Thermodynamic mechanism $\Delta^{LH}T = (\theta_C - \theta e_C) - (\theta_B - \theta e_B)$; (iii) Sensible heat flux and Radiative heating $\Delta^{SH}T + \Delta^{RH}T = \theta e_C - \theta e_B$; (iv) Pressure gradient $\Delta^{\Delta P}T = T_C - \theta_C$. Foehn warming is the temperature change $\Delta^{F}T = T_C - T_A$, the sum of the above contributions.

Data availability

All data used in this study are publicly accessible from these websites: Integrated Surface Database: https://www.ncei.noaa.gov/pub/data/noaa/isd-lite/ and ERA5 dataset: https://cds.climate.copernicus.eu/cdsapp#!/dataset/reanalysis-era5-pressure-levels?tab=form https://cds.climate.copernicus.eu/cdsapp#!/dataset/reanalysis-era5-single-levels?tab=form https://apps.ecmwf.int/data-catalogues/era5/?stream=oper&levtype=ml&expver=1&month=feb&year=2020&type=fc&class=ea

Code availability

All codes used in this study are available upon request.

Received: 16 February 2021; Accepted: 8 June 2021;

References

1. Steig, E. J. et al. Warming of the Antarctic ice-sheet surface since the 1957 International Geophysical Year. *Nature* **457**, 459–462 (2009).
2. Franzke, C. Significant reduction of cold temperature extremes at Faraday/Vernadsky station in the Antarctic Peninsula. *Int. J. Climatol.* **33**, 1070–1078 (2013).
3. Turner, J. et al. Absence of 21st century warming on Antarctic Peninsula consistent with natural variability. *Nature* **535**, 411–415 (2016).
4. Oliva, M. F. et al. Recent regional climate cooling on the Antarctic Peninsula and associated impacts on the cryosphere. *Sci. Total Environ.* **580**, 210–223 (2017).
5. Scambos, T. et al. Ice shelf disintegration by plate bending and hydro-fracture: satellite observations and model results of the 2008 Wilkins ice shelf break-ups. *Earth Planet. Sci. Lett.* **280**, 51–60 (2009).
6. Cook, A. J. & Vaughan, D. G. Overview of areal changes of the ice shelves on the Antarctic Peninsula over the past 50 years. *Cryosphere* **4**, 77–98 (2010).
7. Gutt, J. et al. Biodiversity change after climate-induced ice-shelf collapse in the Antarctic. *Deep Sea Res., Part II* **58**, 74–83 (2011).
8. Rebesco, M. et al. Boundary condition of grounding lines prior to collapse, Larsen-B Ice Shelf, Antarctica. *Science* **345**, 1354–1358 (2014).
9. Schannwell, C., Barrand, N. E. & Radić, V. Future sea-level rise from tidewater and ice-shelf tributary glaciers of the Antarctic Peninsula. *Earth Planet. Sci. Lett.* **453**, 161–170 (2016).
10. King, J. C. & Turner, J. Antarctic meteorology and climatology (Cambridge University Press, 2009).
11. Bozkurt, D. et al. Recent near-surface temperature trends in the Antarctic Peninsula from observed, reanalysis and regional climate model data. *Adv. Atmos. Sci.* **37**, 1–17 (2020).
12. Clem, K. R. & Fogt, R. L. South Pacific circulation changes and the connection to the tropics and regional Antarctic warming in austral spring, 1979-2012. *J. Geophys. Res. Atmos.* **120**, 2773–2792 (2015).
13. Turner, J. et al. Antarctic temperature variability and change from station data. *Int. J. Climatol.* **40**, 1–22 (2019).
14. Ding, Q. & Steig, E. J. Temperature change on the Antarctic Peninsula linked to the tropical pacific. *J. Clim.* **26**, 7570–7585 (2013).
15. Marshall, G. J., Orr, A., Van Lipzig, N. P. M. & King, J. C. The impact of a changing southern Hemisphere Annular Mode on Antarctic peninsula summer temperatures. *J. Clim.* **19**, 5388–5403 (2006).
16. Orr, A. et al. Characteristics of summer airflow over the Antarctic Peninsula in response to recent strengthening of westerly circumpolar winds. *J. Atmos. Sci.* **65**, 1396–1413 (2008).
17. Clem, K. R., Renwick, J. A., McGregor, J. & Fogt, R. L. The relative influence of ENSO and SAM on Antarctic Peninsula climate. *J. Geophys. Res. Atmos.* **121**, 9324–9341 (2016).
18. Cape, M. R. et al. Foehn winds link climate-driven warming to ice shelf evolution in Antarctica. *J. Geophys. Res. Atmos.* **120**, 11037–11057 (2015).
19. Turton, J. V., Kirchgaessner, A., Ross, A. N. & King, J. C. The spatial distribution and temporal variability of föhn winds over the Larsen C ice shelf, Antarctica. *Q J R Meteorol. Soc.* **144**, 1169–1178 (2018).
20. Välisuo, I., Vihma, T. & King, J. C. Surface energy budget on Larsen and Wilkins ice shelves in the Antarctic Peninsula: results based on reanalyses in 1989-2010. *Cryosphere* **8**, 1519–1538 (2014).
21. Elvidge, A. D. et al. Atmospheric drivers of melt on Larsen C Ice Shelf: surface energy budget regimes and the impact of foehn. *J. Geophys. Res.: Atmos.* **125**, 1–25 (2020).
22. Stastna, V. Spatio-temporal changes in surface air temperature in the region of the northern Antarctic Peninsula and south Shetland islands during 1950–2003. *Polar Sci.* **4**, 18–33 (2010).
23. Mulvaney, R. et al. Recent Antarctic Peninsula warming relative to holocene climate and ice-shelf history. *Nature* **489**, 141–144 (2012).
24. Skansi, M. et al. Evaluating highest temperature extremes in the Antarctic. *Eos* **98**, 18–23 (2017).
25. Bozkurt, D., Rondanelli, R., Marin, J. C. & Garreaud, R. Foehn event triggered by an atmospheric river underlies record-setting temperature along continental Antarctica. *J. Geophys. Res.: Atmos.* **123**, 3871–3892 (2018).
26. Bevan, S., Luckman, A., Hendon, H. & Wang, G. Larsen C Ice Shelf surface melt is a 40-year record high. *Cryosphere* **14**, 3551–3564 (2020).
27. Banwell, A. F. et al. The 32-year record-high surface melt in 2019/2020 on the northern George VI Ice Shelf, Antarctic Peninsula. *Cryosphere* **15**, 909–925 (2021).
28. Holton, J. R. & Hakim, G. J. In *An Introduction to Dynamic Meteorology* 5th edn, (eds Holton, J. R. & Hakim, G. J.) 69–70 (Academic Press, 2013).
29. Elvidge, A. D. & Renfrew, I. A. The causes of foehn warming in the lee of mountains. *Bullet. Am. Meteorol. Soc.* **97**, 455–466 (2016).
30. Carrasco, J. F. Contextualizing the 1997 warm event observed at patriot hills in the interior of west Antarctica. *Polar Res.* **37**, 1547041 (2018).
31. Smith, A., Lott, N. & Vose, R. The Integrated Surface Database: recent Developments and Partnerships. *Bullet. Am. Meteorol. Soc.* **92**, 704–708 (2011).
32. Lott, N., Baldwin, R. & Jones, P. *The FCC Integrated Surface Hourly Database: A New Resource of Global Climate Data.* (National Climatic Data Center, 2001).
33. Dai, A. Recent climatology, variability, and trends in global surface humidity. *J. Clim.* **19**, 3589–3606 (2006).
34. Willett, K. M., Jones, P. D., Gillett, N. P. & Thorne, P. W. Recent changes in surface humidity: development of the hadcruh dataset. *J. Clim.* **21**, 5364–5383 (2008).
35. Wang, K. C. & Zhou, C. Regional contrasts of the warming rate over land significantly depend on the calculation methods of mean air temperature. *Sci. Rep.* **5**, 12324 (2015).
36. Copernicus Climate Change Service (C3S), 2017. ERA5: Fifth Generation of ECMWF Atmospheric Reanalyses of the Global Climate. Copernicus Climate Change Service Climate Data Store (CDS). (https://cds.climate.copernicus.eu/) (Accessed: 15 October 2020)
37. Hersbach, H. et al. The ERA5 global reanalysis. *Q J R Meteorol. Soc.* **146**, 1999–2049 (2020).

38. Tetzner, D., Thomas, E. & Allen, C. A Validation of ERA5 Reanalysis Data in the Southern Antarctic Peninsula—Ellsworth Land Region, and Its Implications for Ice Core Studies. *Geosciences* **9**, 289 (2019).
39. Gossart, A. et al. An evaluation of surface climatology in state-of-the-art reanalyses over the Antarctic Ice Sheet. *J. Clim.* **32**, 6899–6915 (2019).
40. Dong, X. et al. Robustness of the recent global atmospheric reanalyses for Antarctic near-surface wind speed climatology. *J. Clim.* **33**, 4027–4043 (2020).
41. Seibert, P. South foehn studies since the ALPEX experiment. *Meteor. Atmos. Phys.* **43**,91–103 (1990).
42. Mahrt, L. & Paumier, J. Heat transport in the atmospheric boundary layer. *J. Atmos. Sci.* **41**, 3061–3075 (2010).
43. Vihma, T., Tuovinen, E. & Savijärvi, H. Interaction of katabatic winds and near-surface temperatures in the Antarctic. *J. Geophys. Res.* **116**, D21119 (2011).
44. Stein, A. F. et al. NOAA's HYSPLIT Atmospheric Transport and Dispersion Modeling System. *Bull. Amer. Meteor. Soc.* **96**, 2059–2077 (2015).
45. Stunder, B. J. B. An assessment of the quality of forecast trajectories. *J. Appl. Meteor.* **35**, 1319–1331 (1996).

Acknowledgements

This study is supported by the National Natural Science Foundation of China (No. 41941009, 41922044, 42075028), the Guangdong Basic and Applied Basic Research Foundation (No. 2020B1515020025), the Fundamental Research Funds for the Central Universities (No. 19lgzd07), the Academy of Finland (No. 304345), ANID-CONICYT-PAI-77190080, ANID-PIA-Anillo INACH ACT192057 and ANID-FONDECYT-11200101. We thank the European Centre for Medium-Range Weather Forecasts (ECMWF) for the ERA5 reanalysis data, the NOAA's Air Resources Laboratory (ARL) for the Hybrid Single-Particle Lagrangian Integrated Trajectory (HYSPLIT) model. This is a contribution to the Year of Polar Prediction (YOPP), a flagship activity of the Polar Prediction Project (PPP), initiated by the World Weather Research Programme (WWRP) of the World Meteorological Organization (WMO). We acknowledge the WMO WWRP for its role in coordinating this international research activity.

Author contributions

Q.Y. conceived the idea for the study; L.Y. and T.V. provided the diabatic heating analysis; K.L. contributed to the section of atmospheric river; D.B. contributed to the section of foehn effect; X.H. contributed to the interpretation of the results; M.X. downloaded the data, performed the calculations, produced the figures and wrote the paper with help from all the co-authors.

Competing interests

The authors declare no competing interests.

Additional information

Supplementary information The online version contains supplementary material available at https://doi.org/10.1038/s43247-021-00203-w.

Correspondence and requests for materials should be addressed to Q.Y.

Peer review information Communications Earth & Environment thanks the anonymous reviewers for their contribution to the peer review of this work. Primary handling editors: Heike Langenberg. Peer reviewer reports are available.